Supporting Information

Organo-Interhalogen Chemistry Enables High-Voltage Bromine Redox for Stable Zinc Batteries

Haolong Huang,[a] Zhiheng Shi,[a] Liting Chen,[a] Jintu Qi,[a] Zhenfeng Feng,[a] Guigui Liu,[a] Minghui Ye,[a,b] Yufei Zhang,[a,b] Zhipeng Wen,[a,b] Xiaoqing Liu,[a,b] Yue Wei,[c] Yongchao Tang,[*a,b] and Cheng Chao Li[*a,b]

[a] H. Huang, Y. Tang, Z. Shi, L. Chen, J. Qi, Z. Feng, G. Liu, Z. Wen, M. Ye, Y. Zhang, X. Liu, C. C. Li

School of Chemical Engineering and Light Industry, Guangdong University of Technology, Guangzhou 510006 (China)

**E-mail: licc@gdut.edu.cn;* tyc@gdut.edu.cn

[b] Y. Tang, M. Ye, Y. Zhang, Z. Wen, X. Liu, C. C. Li

Guangdong Provincial Laboratory of Chemistry and Fine Chemical Engineering Jieyang Center, Jieyang 515200 (China)

[c] Y. Wei

School of Environment and Civil Engineering, Dongguan University of Technology, Dongguan, Guangdong 523808 (China)

Experimental section

Preparation of aqueous electrolytes: 2 M (mol L^{-1}) $ZnSO_4$ solution (ZS) was prepared by adding 0.323 g $ZnSO_4$ to 1 mL of deionized water and stirring for 1 h at room temperature. Then, 0.2 M $ZnCl_2$ and 0.4 M CA were added to the as-prepared ZS solutions, respectively, and stirred for 2~4 h at room temperature to obtain ZC electrolytes and CA electrolytes. Similarly, other additives (e.g., CP, ClACE, MCA, and CAN) were also introduced into electrolytes at 0.4 M concentration for comparative investigations.

Fabrication of $TBABr_3$ electrode: $TBABr_3$, KB, and polyvinylidene fluoride (PVDF) with a ratio of 6:3:1 in methyl-2-pyrrolidinone (NMP) solvent were mixed to form a homogeneous slurry. Subsequently, this slurry was evenly coated onto carbon fiber cloth (CFC), then drying at 45 °C for 12 h. The effective mass loading of active bromine is controlled around 1.0-2.0 mg cm^{-2}.

Preparation of Br_3^- and Br^+: Br_3^- solution was prepared by the reaction between $NaBrO_3$ and HBr[1]: $NaBrO_3 + 8Br^- + 6H^+ \rightarrow 3Br_3^- + 3H_2O$. $BrCl_2^-$ solution was prepared through a method reported as follows[2]: $Cl_2 + Br^- \rightarrow BrCl_2^-$.

Electrochemical measurements: Electrochemical tests were conducted using CR2032 coin cells assembled in ambient environment with a cut-off voltage of 0.5-2.15 V. For the coin cell assembly, 120 μL ZS with different additives were used as the electrolytes, Zn foil with 0.1 mm thickness was used as the anode, $TBABr_3$ electrode was used as the cathodes, and glass fiber membrane (Whatman) was used as the separators. The mass loading of cathode active material is controlled to *ca.* 2 mg cm^{-2}. The galvanostatic charge-discharge were performed on the Neware electrochemical test system (CT-4008-10V 50mA-164, Shenzhen, China). The CV, LSV curves, and EIS plots were tested on a Gamry electrochemical workstation, and the frequency of EIS ranged from 100 kHz to 0.1 Hz.

Characterization methods: UV-vis spectra were collected using a Shimadzu UV-visible near-infrared spectrophotometer. Infrared spectra were recorded on an FT-IR spectrometer (Nicolet iS50R, Thermo Scientific). Raman spectra (HORIBA, LabRAM HR800) of the samples were measured at room temperature with laser excitation at 532 nm. Sample morphology was observed using a scanning electron microscope (SEM, Hitachi S-3400 N). Surface roughness of the resultant samples was characterized using laser scanning confocal microscopy (LSCM). The ^{1}H and ^{13}C NMR spectra were recorded by a Bruker AVANCE III 500 MHz Superconducting Fourier using $CDCl_3$ as the solvent and trimethylsilane (TMS) as the standard internal substance. For ex-situ ^{1}H and ^{13}C NMR spectra tests, the cathodes with different states of charge (SOC) were soaked in 0.6 mL $CDCl_3$ for 30 min filtered to obtain a clear solution, and then transferred to the NMR tube for analysis. XRD analysis was used to determine the phase structures of the anode samples using a Rigaku instrument (Cu Kα, λ= 1.5418 Å). The chemical states of the electrodes after tests were determined by XPS (Thermo Fisher-Escalab 250Xi), and binding energies were calibrated using carbon (284.8 eV for C 1s). The mass spectrum was conducted on Thermo Fisher Scientific LTQ-Orbitrap XL by electrospray ionization to qualitatively determine the charging product of interhalogen. The in-situ hydrogen fluxes are detected by the airtight battery system equipped with gas chromatography-mass spectrometry. In the battery-gas chromatography quantitative analysis measurement, the airtight battery system is connected to gas chromatography (Agilent GC-2014).

Calculation of the activation energy: The activation energy can be calculated by the Arrhenius equation:

$$\frac{1}{R_{ct}} = A exp(- \frac{E_a}{RT})$$

where R_{ct} is the interfacial resistance, A is the frequency factor, R is the gas constant, and T is the absolute temperature.

Theoretical computations: All the DFT calculations were carried out in the DMol[3] package of Materials Studio. The exchange-correlation energy was computed using generalized gradient approximation (GGA) with the Perdew-Burke-Ernzerhof (PBE).[3] Grimme's DFT-D2 model was also used to take into account Van der Waals interactions.[4] The core electrons were treated with DFT semi-core pseudopotentials. The simulation was conducted with a global orbital cutoff of 5.0 Å and a Fermi smearing of 0.005 Ha (1 Ha= 27.211 eV). The criteria for convergence in geometric optimization and energy calculation were defined with an energy tolerance of 1.0×10^{-5} Ha/atom, a self-consistent field tolerance of 1.0×10^{-6} Ha/atom, a maximum force tolerance of 0.002 Ha/Å, and a maximum displacement tolerance of 0.005 Å. The Gibbs free energy of reaction ($\Delta G_{reaction}$) is typically calculated by determining the free energy of the reactants and products. The formula for the reaction free energy is:

$$\triangle G_{reaction} = \sum G_{products} - \sum G_{reactants}$$

Where $\sum G_{products}$ stands for the free energy of the products and $\sum G_{reactants}$ stands for the free energy of the reactants.

Calculation of energy density and power density: The energy density (*E*) delivered by the battery can be calculated by integrating the voltage (*V*) over the specific capacity (*Q*):

$$Energy\ density\ (E) = \int_{intial}^{final} V(Q)\,dQ \Big/ m$$

where, *V(Q)* is the voltage as a function of capacity; $Q_{initial}$ and Q_{final} are the start and end points of the discharge curve; *m* is the mass of the bromine active material.

The power density (*P*) delivered by the battery can be calculated using the energy density (*E*) and discharge time (*t*):

$$Power\ density\ (P) = E/t$$

where, *E* is the energy density and *t* is the discharge time.

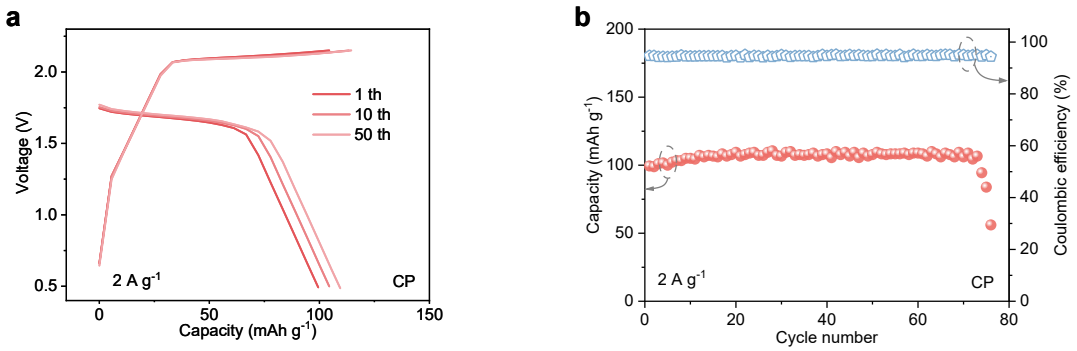

Fig. S1. (a) GCD curves and (b) long-term cycling performance of Zn||$TBABr_3$ batteries with CP electrolyte at 2 A g^{-1}.

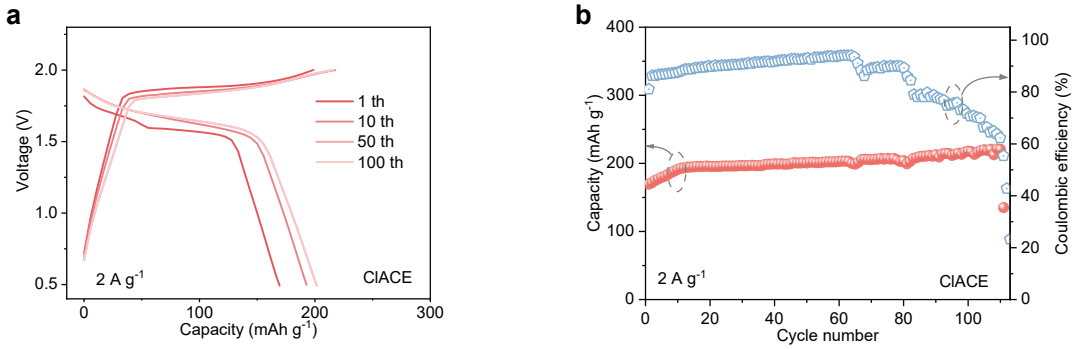

Fig. S2. (a) GCD curves and (b) long-term cycling performance of Zn||$TBABr_3$ batteries with ClACE electrolyte at 2 A g^{-1}.

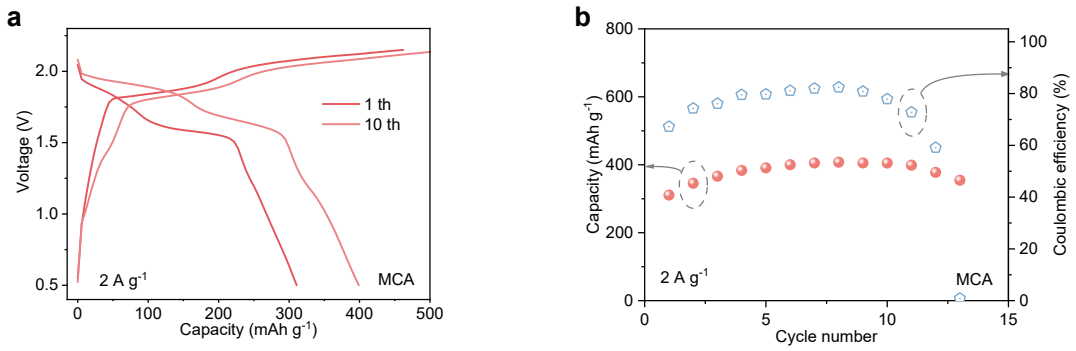

Fig. S3. (a) GCD curves and (b) long-term cycling performance of Zn||$TBABr_3$ batteries with MCA electrolyte at 2 A g^{-1}.

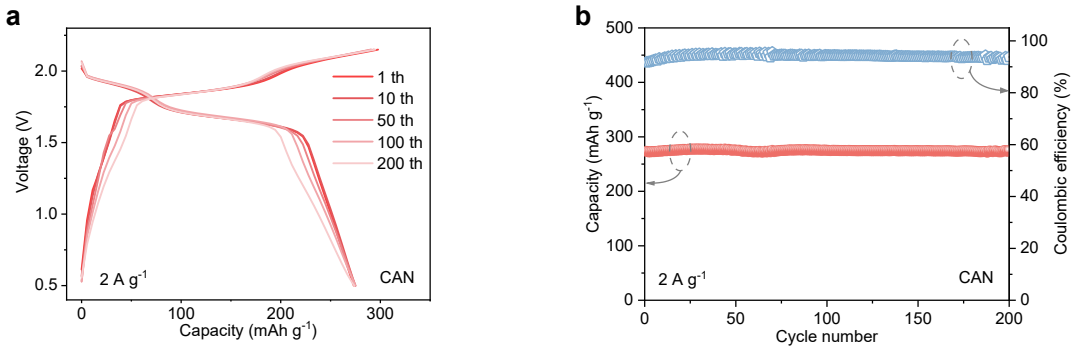

Fig. S4. (a) GCD curves and (b) long-term cycling performance of Zn||$TBABr_3$ batteries with CAN electrolyte at 2 A g^{-1}.

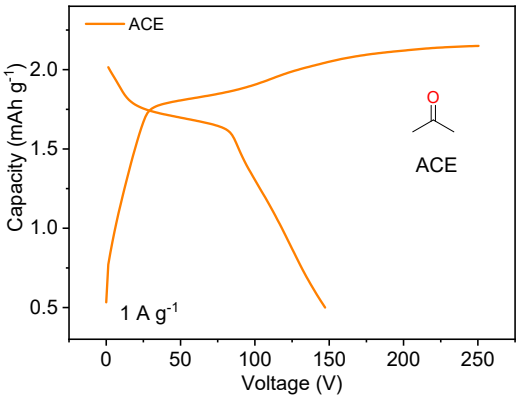

Fig. S5. GCD curves of Zn||$TABBr_3$ batteries with ACE electrolyte at 1 A g^{-1}.

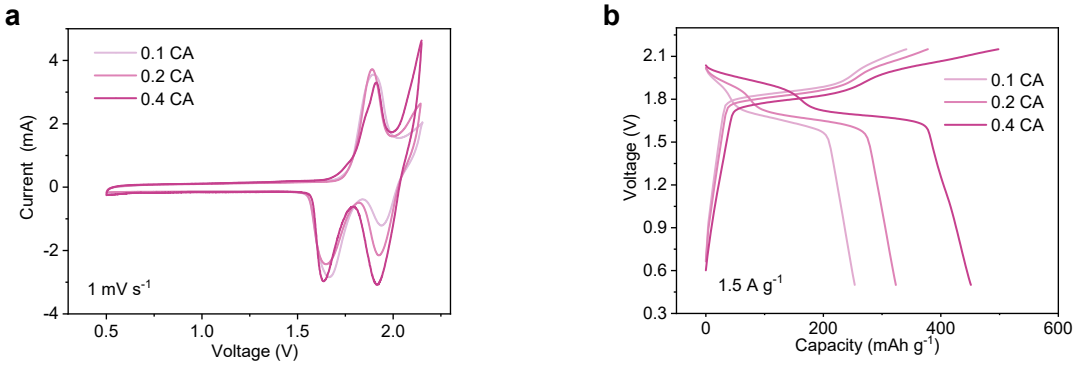

Fig. S6. (a) CV of Zn||$TABBr_3$ batteries in electrolytes with different CA concentrations at 1 mV s^{-1} and (b) GCD curves at 1.5 A g^{-1}.

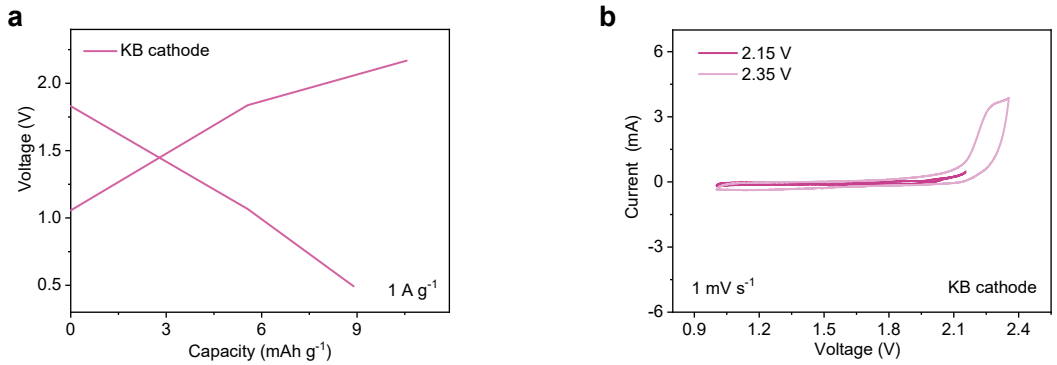

Fig. S7. (a) GCD curves of the Zn||KB battery in CA electrolyte. (b) CV curves of the Zn||KB battery in CA electrolyte at the upper voltage limits of 2.15 V and 2.35 V.

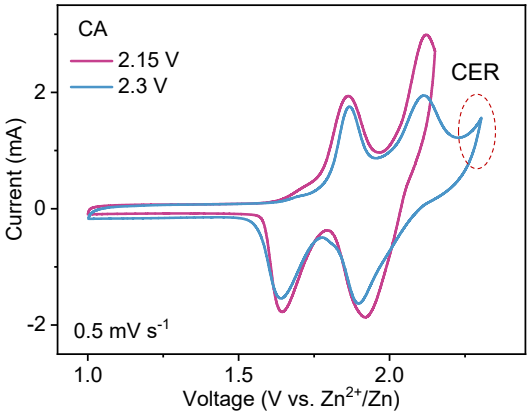

Fig. S8. CV of Zn||$TBABr_3$ batteries with CA electrolyte with different voltage ranges.

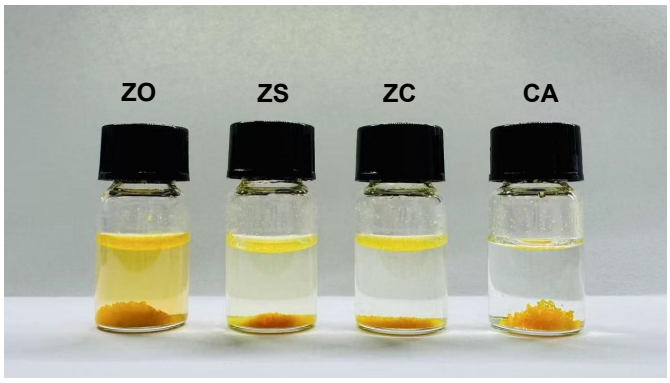

Fig. S9. Photographs of $TBABr_3$ in four electrolytes: ZO, ZS, ZC, and CA electrolytes; 2 M $Zn(OTf)_2$ was denoted as ZO.

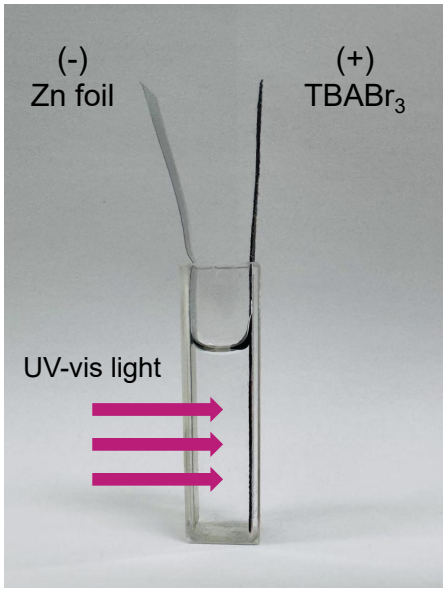

Fig. S10. The cuvette cell for in situ UV-Vis spectral characterization.

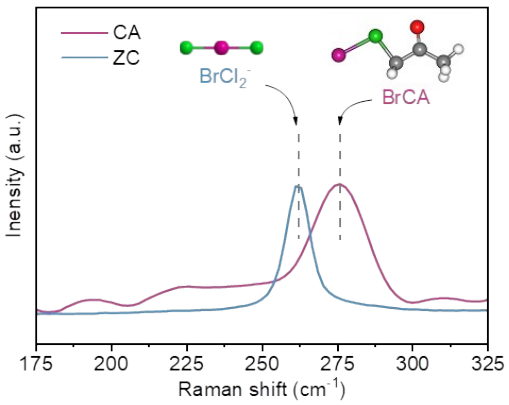

Fig. S11. Raman spectra of the battery cathodes charged to 2.15 V using CA and ZC electrolytes.

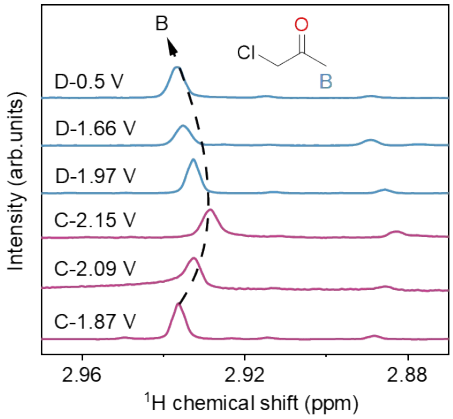

Fig. S12. *Ex-situ* ^{1}H NMR spectra of cathode during GCD with CA.

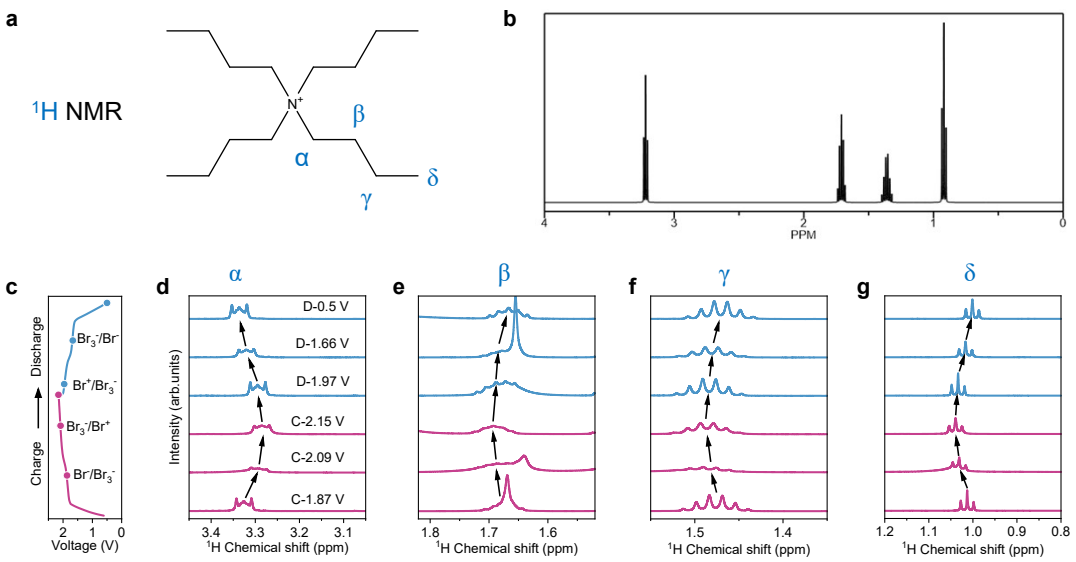

Fig. S13. (a) Molecular structures and (b) ^{1}H NMR spectrum of TBA^{+}. (c) GCD curves of Zn||TBABr$_3$ battery with CA electrolyte. (d-g) ^{1}H NMR spectra of TBA^{+} at different states of charge: (d) peak α, (e) peak β, (f) peak γ, (g) peak δ.

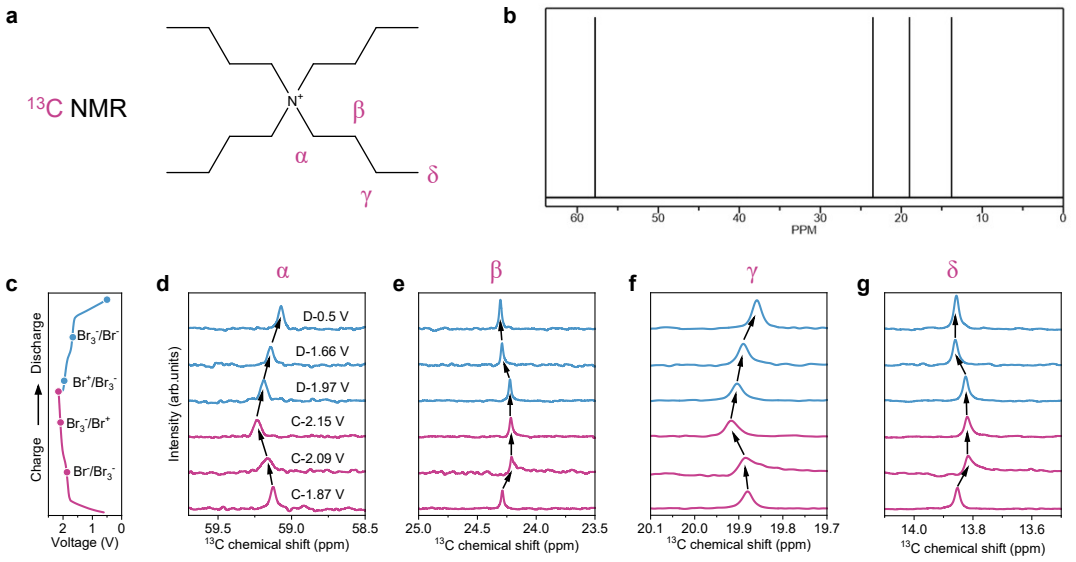

Fig. S14. (a) Molecular structures and (b) ^{13}C NMR spectrum of TBA^{+}. (c) GCD curves of Zn||TBABr$_3$ battery with CA electrolyte. (d-g) ^{1}H NMR spectra of TBA^{+} at different states of charge: (d) peak α, (e) peak β, (f) peak γ, (g) peak δ.

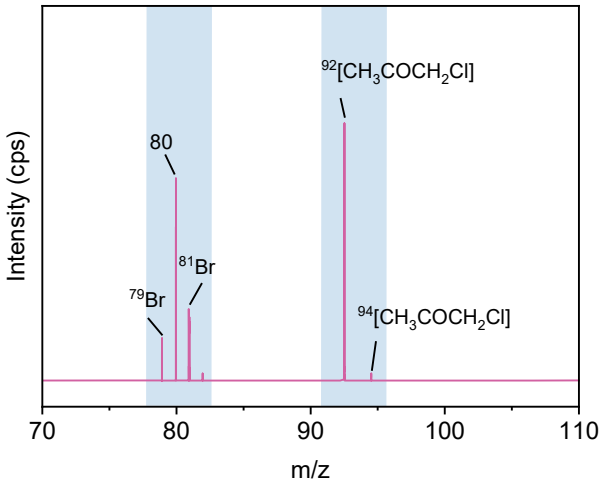

Fig. S15. Mass spectrum of cathodes at of charge to 2.15 V in CA electrolyte.

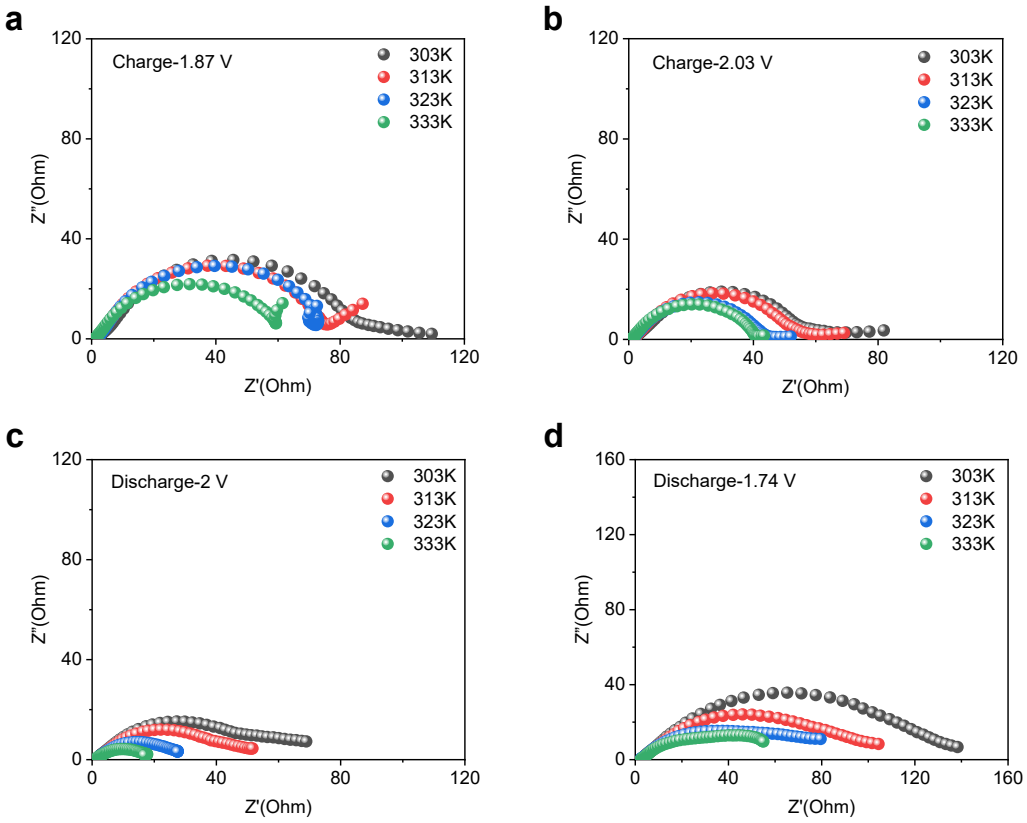

Fig. S16. EIS spectra of Zn||$TBABr_3$ batteries with ZC electrolytes at different temperatures and charged/discharged states.

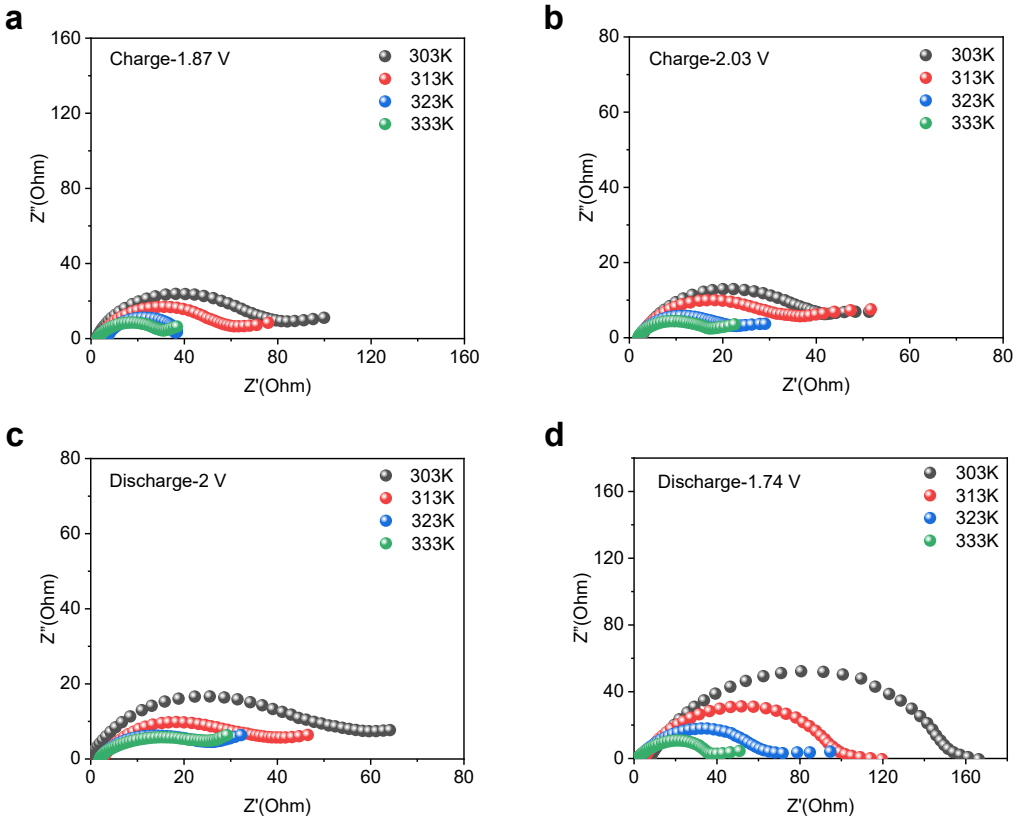

Fig. S17. EIS spectra of Zn||$TBABr_3$ batteries with CA electrolytes at different temperatures and charged/discharged states.

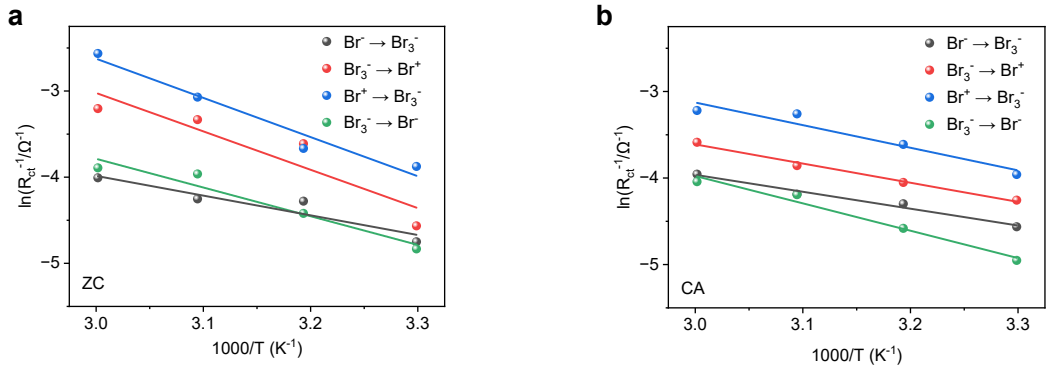

Fig. S18. Arrhenius plots of Zn||$TBABr_3$ batteries with (a) ZC and (b) CA electrolytes at different temperatures and charged/discharged states.

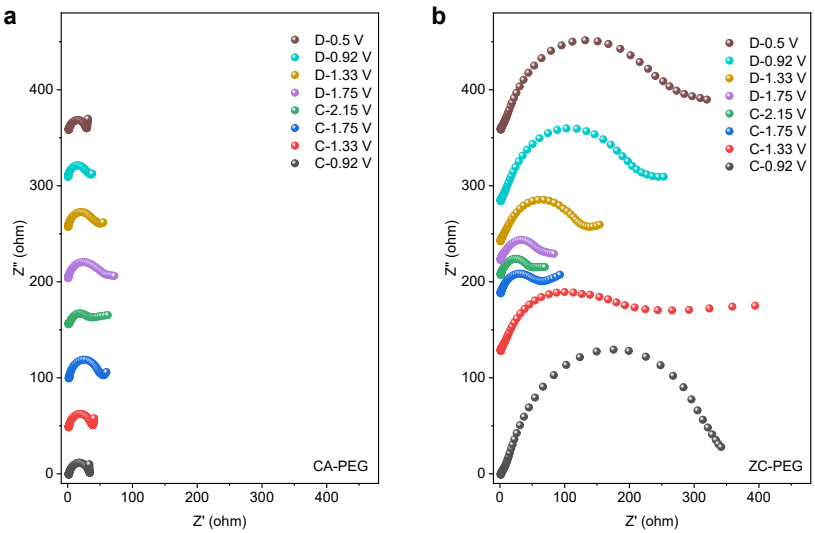

Fig. S19. Nyquist plots for Zn||$TBABr_3$ batteries using (a) CA-PEG and (b) ZC-PEG electrolytes obtained by in-situ EIS tests.

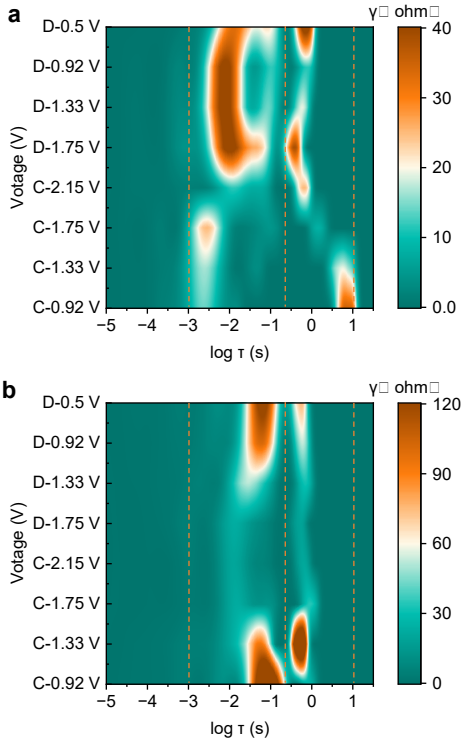

Fig. S20. DRT plots for Zn||$TBABr_3$ batteries with (a) CA-PEG and (b) ZC-PEG electrolytes at different potentials.

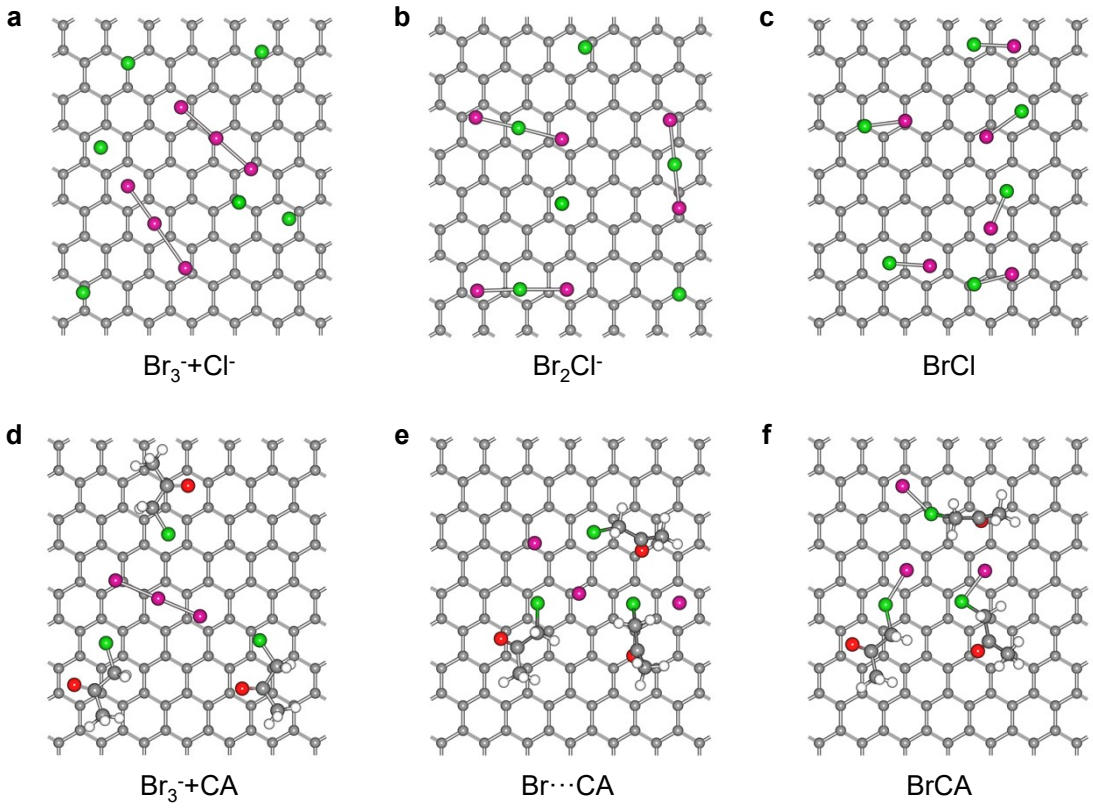

Fig. S21. The Gibbs free energy model for the structures of key species involved in CA- and $ZnCl_2$-mediated Br_3^-/Br^+ redox.

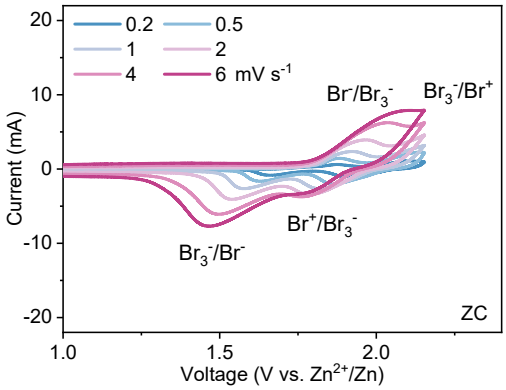

Fig. S22. CV curves of Zn||$TBABr_3$ batteries with ZC electrolytes at scan rates of 0.2-6 mV s^{-1}.

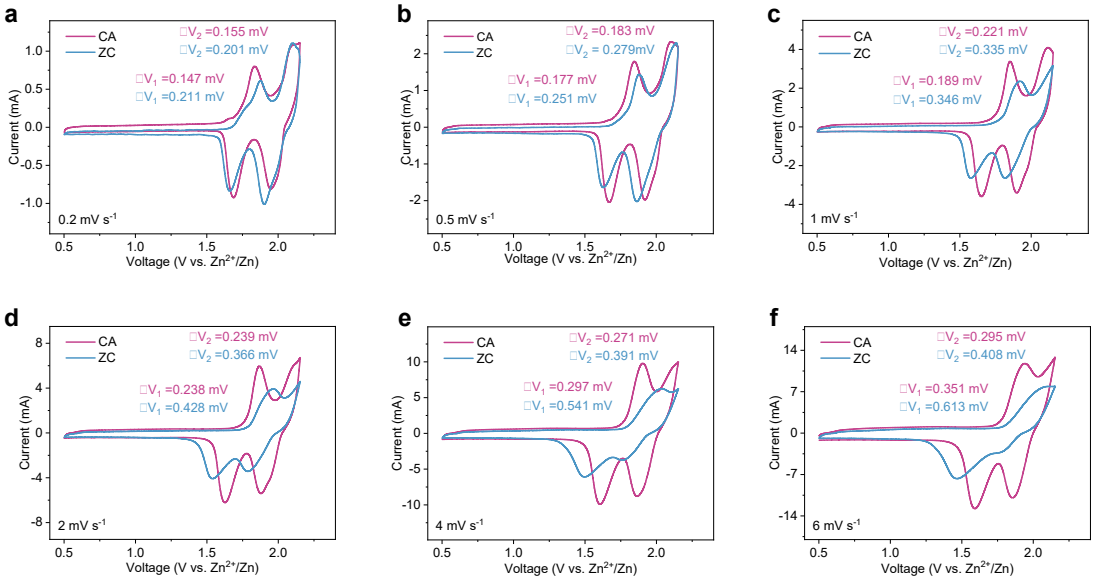

Fig. S23. (a-f) Comparison of CV curves of Zn||$TABBr_3$ batteries with ZC and CA electrolytes at different scan rates; $\triangle V_1$ and $\triangle V_2$ respectively represent the voltage difference between the oxidation peak and the reduction peak of Br^-/Br_3^- and Br_3^-/Br^+.

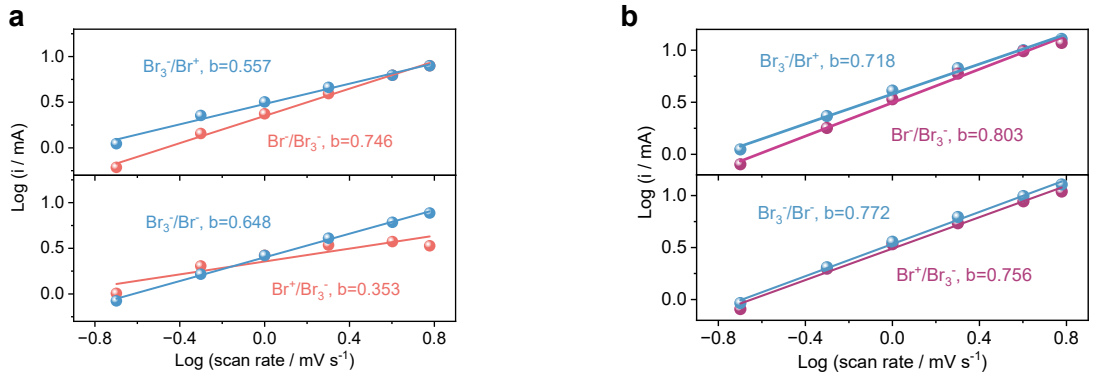

Fig. S24. Logi versus logν plots of the current response with ZC and CA electrolytes.

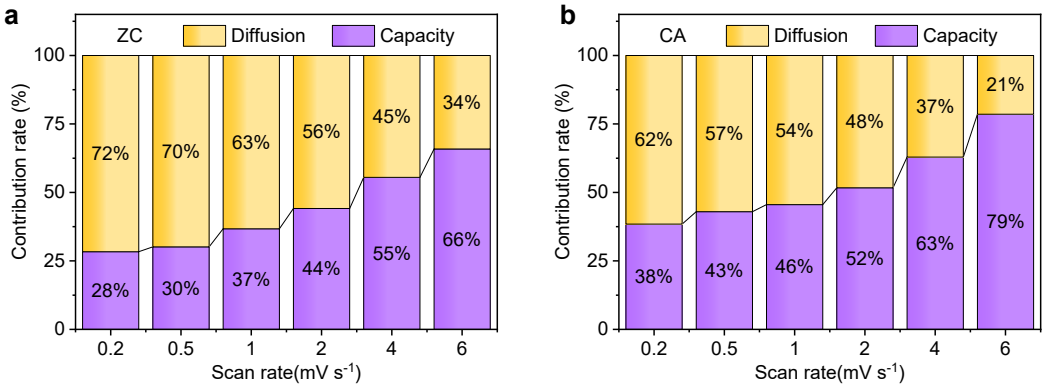

Fig. S25. Diffusion-controlled and capacitive contributions of Zn||$TABABr_3$ batteries at different scan rates: (a) with ZC electrolyte; (b) with CA electrolyte.

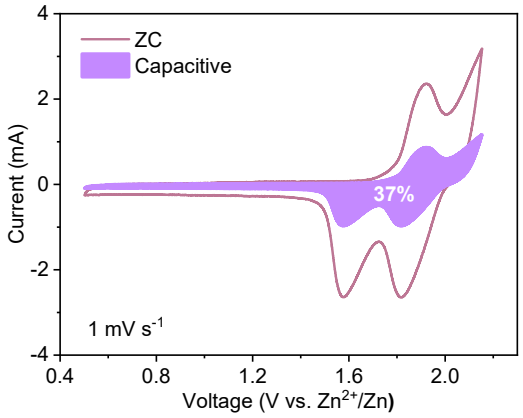

Fig. S26. CV curves and corresponding capacitive contribution (37%, shaded part) of Zn||$TABABr_3$ batteries with ZC electrolyte at 1 mV s^{-1}.

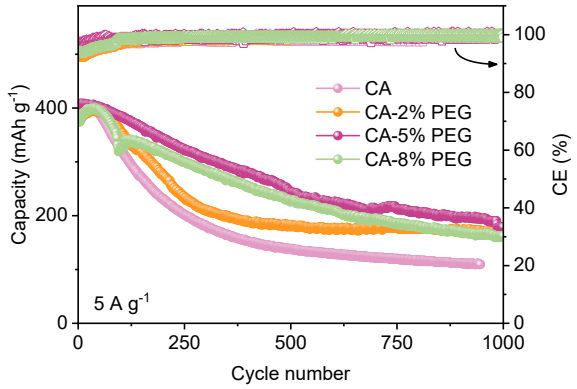

Fig. S27. Cycling stability of Zn||$TBABr_3$ batteries in CA electrolyte with different PEG 200 concentrations at current densities of 5 A g^{-1}.

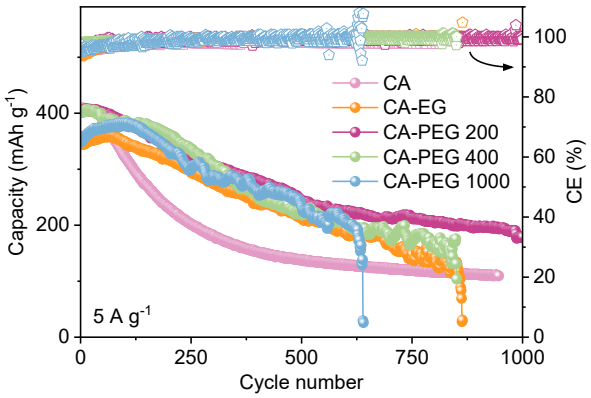

Fig. S28. Cycling stability of Zn||$TBABr_3$ batteries in CA electrolytes with 5 wt% EG and PEG with different molecular weights (200, 400, and 1000 g mol^{-1}) at current densities of 5 A g^{-1}.

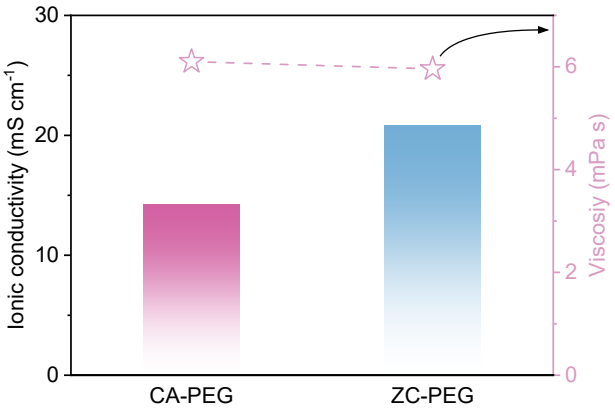

Fig. S29. The ionic conductivity and viscosity of the CA-PEG and ZC-PEG electrolytes.

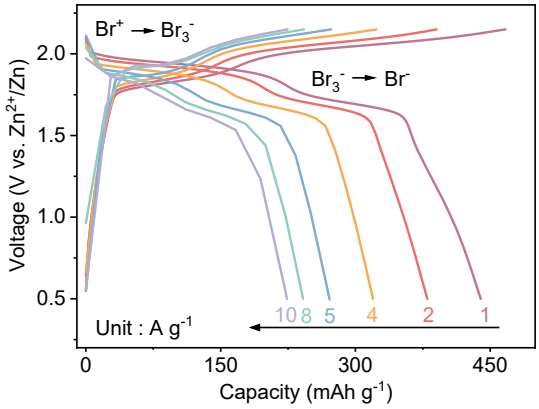

Fig. S30. GCD curves in ZC-PEG electrolytes at current densities of 1, 2, 4, 5, 8, and 10 A g^{-1}.

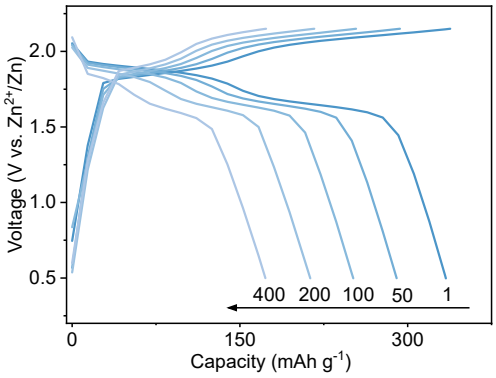

Fig. S31. The GCD curves in ZC-PEG electrolytes at 5 A g^{-1}.

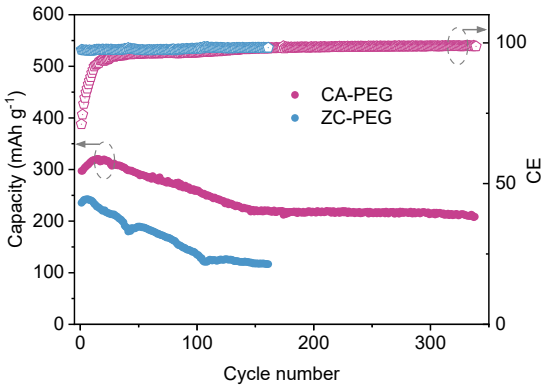

Fig. S32 Cycling performance of full batteries at current densities of 10 A g^{-1} in CA-PEG and ZC-PEG electrolytes.

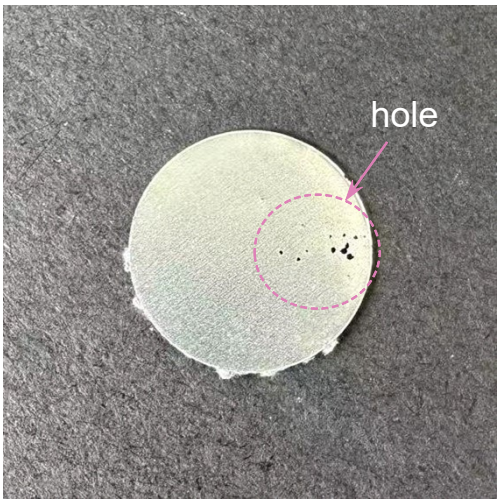

Fig. S33. Photographs of the perforation on the reverse side of the Zn anode after cycling of the Zn||$TBABr_3$ battery using ZC-PEG electrolyte.

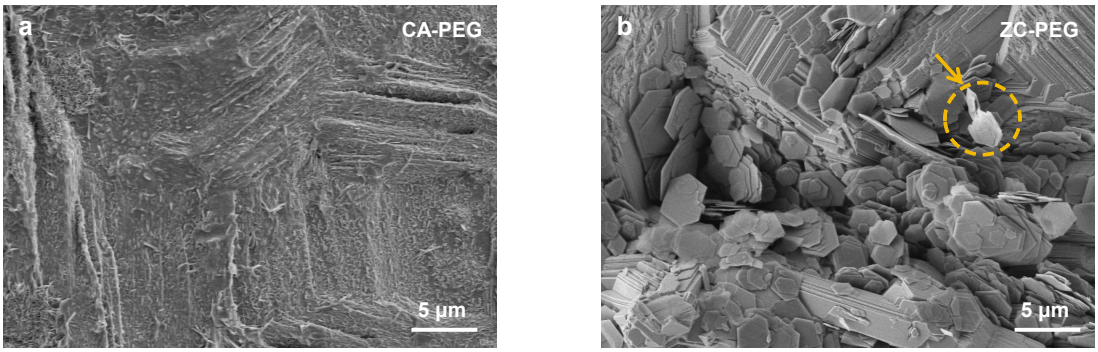

Fig. S34. SEM images of Zn anodes cycled in Zn||Zn symmetric cells at 5 mAh cm^{-2}, 1 mA cm^{-2} after 250 cycles with different electrolytes: (a) ZC-PEG and (b) CA-PEG.

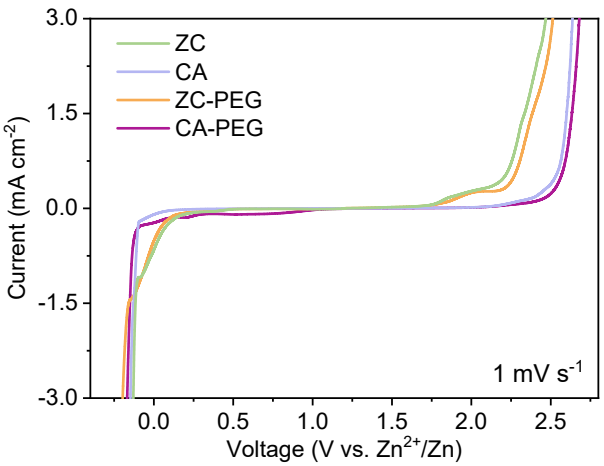

Fig. S35. LSV profiles in ZC-PEG and CA-PEG electrolytes at 1 mV s^{-1}.

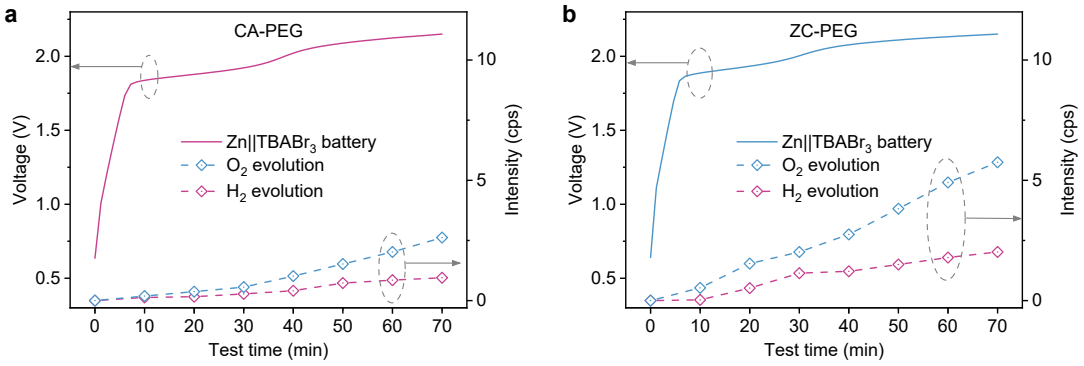

Fig. S36. O_2 and H_2 evolution during the cycling process of Zn||$TBABr_3$ batteries using a) CA-PEG and b) ZC-PEG electrolytes was investigated by GC-MS.

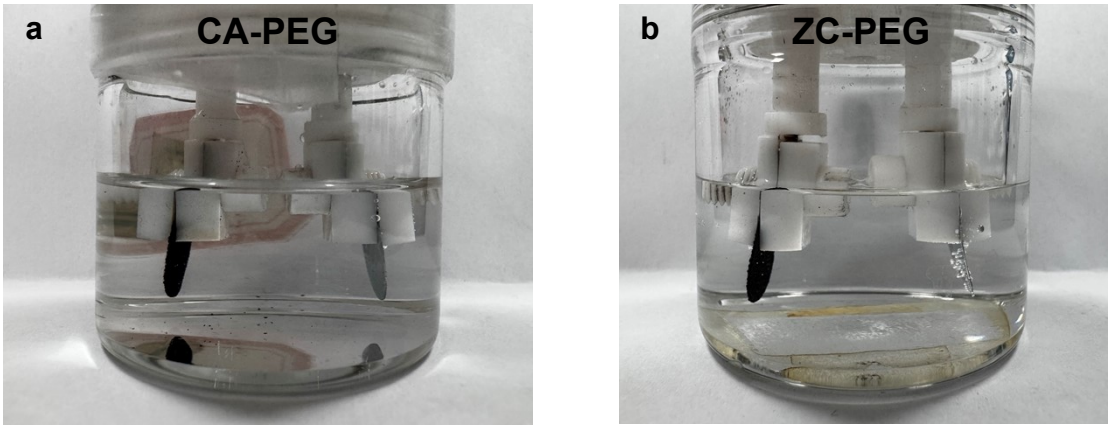

Fig. S37. Optical photos of the beaker batteries used for GC-MS tests after cyclic testing in a) CA-PEG and b) ZC-PEG.

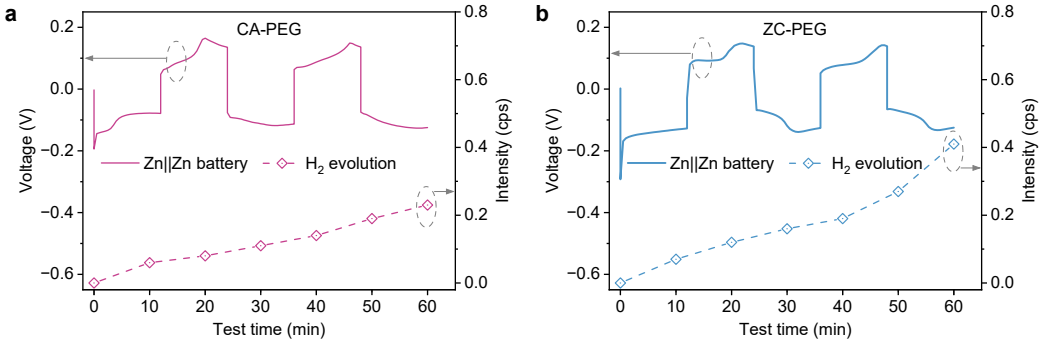

Fig. S38. H_2 evolution during the cycling process of Zn||Zn batteries using a) CA-PEG and b) ZC-PEG electrolytes was investigated by GC-MS.

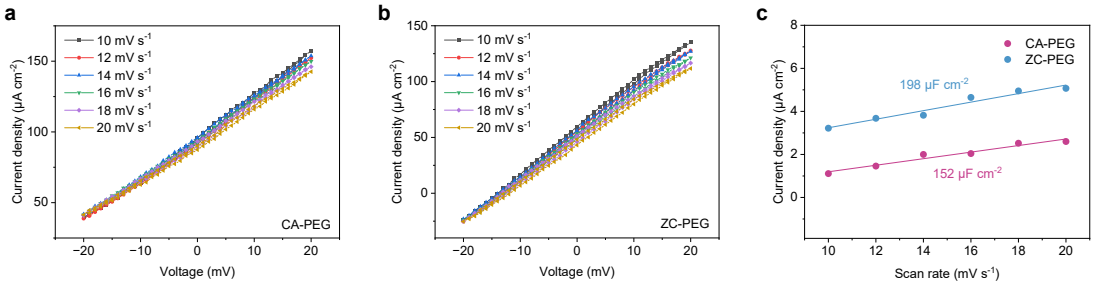

Fig. S39 CV curve of the Zn||Zn symmetric batteries at 10-20 mV s^{-1} with (a) CA-PEG and (b) ZC-PEG. (c) The electric double layer capacitance with different electrolytes.

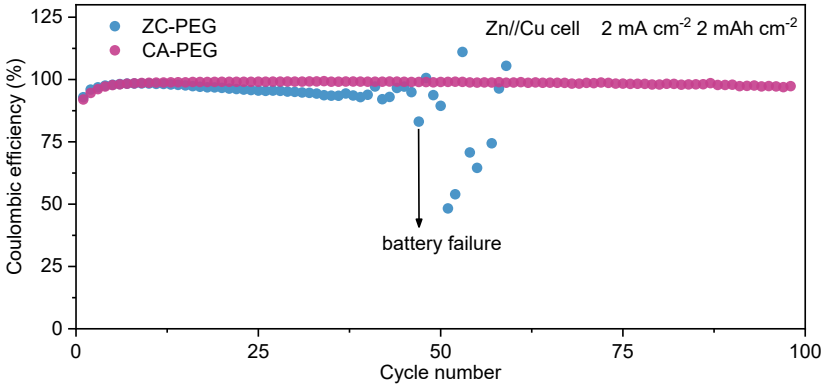

Fig. 40. Cycling performance of Zn||Cu asymmetric cells at 2 mA cm^{-2} with 2 mA h cm^{-2} in ZC-PEG and CA-PEG electrolytes.

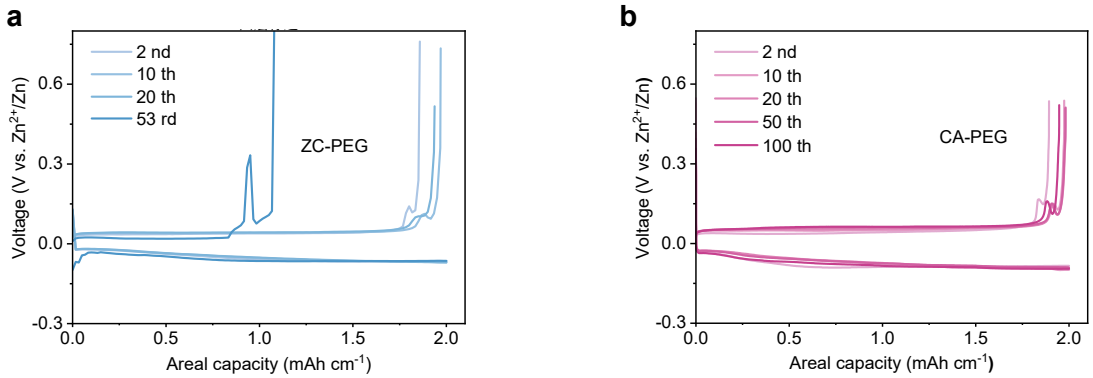

Fig. S41. Charge/discharge profiles corresponding to Zn||Cu asymmetric cells in (a) ZC-PEG and (b) CA-PEG electrolytes.

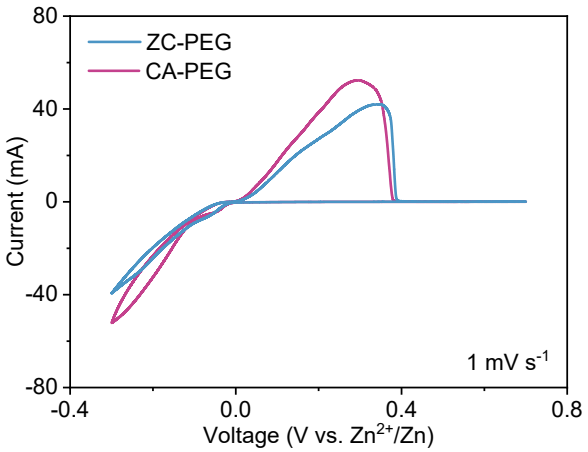

Fig. S42. CV curves of Zn||Cu asymmetric cells at a scan rate of 1 mV s^{-1} in ZC-PEG and CA-PEG electrolytes.

Table S1. Discharge voltage and specific capacity comparison of this work with other cathodes reported previously.

Cathode	Current density (A g^{-1})	Specific Capacity (mAh g^{-1})	Discharge voltage (V)	Ref.
I^-/I^0	0.2	210	1.28	[5]
	8	89	1.20	
$I^-/I^0/I^+$	1	446	1.65	[6]
	10	314	1.56	
Br^-/Br_3^-	0.2	334	1.67	[7]
	15	187	1.60	
Mn-based	0.2	318	1.41	[8]
	2.5	173	1.36	
V-based	0.1	388	0.96	[9]
	5	173	0.91	
PBA-based	0.1	101	1.71	[10]
	2	52	1.67	
$Br^-/Br_3^-/BrCl_2^-$	1	439	1.94	Comparison sample
	10	224	1.83	
$Br^-/ Br_3^-/BrCA$	1	508	1.95	This work
	10	331	1.87	

Table S2. Energy densities and power densities comparison of this work with other conversion-type cathodes.

Cathode	Power density ($W\ kg^{-1}$)	Energy density ($Wh\ kg^{-1}$)	mass loading ($mg\ cm^{-2}$)	Ref.
I^-/I^0	662	208	0.8-1.0	[11]
	16994	148		
$I^-/I^0/I^+$	252	463	4	[12]
	3729	217		
Br^-/Br^0	296	404	1.6	[7]
	2102	112		
S^0/S^{4+}	130	404	2	[13]
	6657	193		
S^{2-}/S^0	181	444	2	
	789	78		
$Se^{2-}/Se^0/Se^{4+}$	123	403	3.2	[14]
	1448	113		
$Br^-/Br_3^-/BrCl_2^-$	1963	747	2	Control system
	18605	355		
Br^-/Br_3^-/BrCA	2095	848	2	This work
	19747	529		

References

1 L. Gao, Z. Li, Y. Zou, S. Yin, P. Peng, Y. Shao and X. Liang, *iScience*, 2020, **23**, 101348.

2 C. Chiappe, F. Del Moro and M. Raugi, *Eur. J. Org. Chem.*, 2001, **2001**, 3501–3510.

3 J. P. Perdew, K. Burke and M. Ernzerhof, *Phys. Rev. Lett.*, 1996, **77**, 3865–3868.

4 S. Grimme, J. Antony, S. Ehrlich and H. Krieg, *J. Chem. Phys.*, 2010, **132**, 154104.

5 F. Yang, J. Long, J. A. Yuwono, H. Fei, Y. Fan, P. Li, J. Zou, J. Hao, S. Liu, G. Liang, Y. Lyu, X. Zheng, S. Zhao, K. Davey and Z. Guo, *Energy Environ. Sci.*, 2023, **16**, 4630–4640.

6 W. Zong, J. Li, C. Zhang, Y. Dai, Y. Ouyang, L. Zhang, J. Li, W. Zhang, R. Chen, H. Dong, X. Gao, J. Zhu, I. P. Parkin, P. R. Shearing, F. Lai, K. Amine, T. Liu and G. He, *J. Am. Chem. Soc.*, 2024, **146**, 21377–21388.

7 S. Chen, C. Peng, D. Zhu and C. Zhi, *Adv. Mater.*, 2024, **36**, 2409810.

8 N. Jiang, Y. Zeng, Q. Yang, P. Lu, K. Qu, L. Ye, X. Lu, Z. Liu, X. Li, Y. Tang, J. Cao, S. Chen, C. Zhi and J. Qiu, *Energy Environ. Sci.*, 2024, **17**, 8904–8914.

9 D. Zhang, J. Cao, C. Yang, K. Lolupiman, W. Limphirat, X. Wu, X. Zhang, J. Qin and Y. Huang, *Adv. Energy Mater.*, 2025, **15**, 2404026.

10 Y. Zeng, J. Xu, Y. Wang, S. Li, D. Luan and X. W. (David) Lou, *Angew. Chem. Int. Ed.*, 2022, **61**, e202212031.

11 T. Xiao, J. Yang, B. Zhang, J. Wu, J. Li, W. Mai and H. J. Fan, *Angew. Chem. Int. Ed.*, 2024, **63**, e202318470.

12 L. Chen, S. Huang, Z. Feng, Z. Lin, H. Huang, M. Ye, Y. Zhang, Z. Wen, Y. Tang, X. Liu and C. C. Li, *Angew. Chem. Int. Ed.*, 2025, **64**, e202510737.

13 Z. Chen, Z. Huang, J. Zhu, D. Li, A. Chen, Z. Wei, Y. Wang, N. Li and C. Zhi, *Adv. Mater.*, 2024, **36**, 2402898.

14 L. Ma, Y. Ying, S. Chen, Z. Chen, H. Li, H. Huang, L. Zhao and C. Zhi, *Adv. Energy Mater.*, 2022, **12**, 2201322.